2

Doppler OCT and OCT Angiography for *In Vivo* Imaging of Vascular Physiology

Vivek J. Srinivasan[1], Aaron C. Chan[2] and Edmund Y. Lam[2]
[1]*MGH/MIT/HMS Athinoula A. Martinos Center for Biomedical Imaging, Department of Radiology, Massachusetts General Hospital, Harvard Medical School, Charlestown, Massachusetts*
[2]*Department of Electrical and Electronic Engineering, The University of Hong Kong, Pokfulam Road,*
[1]*U.S.A.*
[2]*Hong Kong*

1. Introduction

Optical imaging methods (Grinvald et al., 1986; Villringer and Chance, 1997; Wilt et al., 2009) have had a significant impact on the field of neuroimaging and are now widely used in studies of both cellular and vascular physiology and pathology. Currently, *in vivo* optical imaging modalities can be broadly classified into two groups: macroscopic methods using diffuse light (optical intrinsic signal imaging (Grinvald et al., 1986), laser Doppler imaging (Dirnagl et al., 1989), laser speckle imaging (Dunn et al., 2001), diffuse optical imaging (Villringer and Chance, 1997), and laminar optical tomography (Hillman et al., 2004)) which achieve spatial resolutions of hundreds of microns to millimeters, and microscopic methods (two photon and confocal microscopy) which achieve micron-scale resolutions. Two-photon microscopy (Denk et al., 1990), in particular, is widely used in structural and functional imaging at the cellular and subcellular levels. While macroscopic imaging methods using diffuse light can achieve high penetration depths and large fields of view, they do not provide high spatial resolution. While two-photon microscopy achieves subcellular spatial resolution, the imaging speed, penetration depth, and field of view are limited.

Optical Coherence Tomography (OCT) (Huang et al., 1991) possesses a unique combination of high imaging speed, penetration depth, field of view, and resolution and therefore occupies an important niche between the macroscopic and microscopic optical imaging technologies discussed above. Relative to the optical imaging technologies currently used for neuroscience research, OCT has several advantages. Firstly, OCT enables volumetric imaging with high spatiotemporal resolution. OCT volumetric imaging requires tens of seconds to a few minutes. By contrast, volumetric imaging with two-photon microscopy typically requires tens of minutes to a few hours. Secondly, OCT achieves high penetration depth. OCT rejects out-of-focus and multiple scattered light, enabling imaging at depths of greater than 1 mm in scattering tissue. By comparison, conventional two-photon microscopy enables imaging depths of approximately 0.5 mm in scattering tissue. Third, OCT can be

performed with long working distance, low numerical aperture (NA) objectives. Because the OCT depth resolution depends on the coherence length of light and not the confocal parameter (depth of field), low NA lenses may be used without sacrificing depth resolution. This contrasts with two-photon microscopy, where high depth resolution and penetration depth in scattering tissue *in vivo* can be achieved only with high-NA water immersion objectives. The use of relatively low NA objectives allows imaging of large fields of view, enabling the synthesis of microscopic and macroscopic information. Fourth, since OCT can measure well-defined volumes using predominantly single scattered light, quantitative assessment of hemodynamic parameters such as blood vessel diameter and blood flow using Doppler algorithms (Chen et al., 1997; Izatt et al., 1997) are possible. Fifth, OCT is performed using intrinsic contrast alone, and does not require the use of dyes or extrinsic contrast agents. This capability is attractive for longitudinal studies where cumulative dye toxicity is a concern.

In this chapter, we describe Doppler OCT and OCT angiography methods for the study of cerebrovascular physiology. We describe OCT technologies and methodologies relevant to *in vivo* imaging of the brain and other organs; with a focus on understanding signal modelling and software algorithms. While the methods and algorithms we describe here are applied to brain imaging, similar techniques can be used to image and quantify vascular physiology in other organ systems.

2. Methods

2.1 OCT Technologies

In conventional "time-domain" OCT, a low coherence light source is used with a Michelson interferometer with a sample arm and a reference arm. The reference path length is varied in time to generate a profile of backscattering or backreflectance vs. depth (Huang et al., 1991), and light is detected with a single photodiode or pair of photodiodes. Since 2003, new Fourier domain OCT detection methods have enabled dramatic increases in sensitivity (Choma et al., 2003; de Boer et al., 2003; Leitgeb et al., 2003) compared to conventional OCT detection methods. These methods are called "Fourier domain" because they detect the interference spectrum and do not require mechanical scanning of the reference path length in time. Fourier domain OCT has two known embodiments. The first embodiment, "spectral / Fourier domain" OCT (Fercher et al., 1995), uses a broadband light source and a high-speed, high resolution spectrometer for detection. The second embodiment, "swept source / Fourier domain" OCT (Golubovic et al., 1997; Yun et al., 2003), uses a frequency tunable light source and a photodiode or pair of photodiodes for detection.

The Doppler OCT and OCT angiography techniques described in this chapter may be applied to any of the OCT embodiments, provided that phase-resolved axial scan information is available. Fourier domain OCT techniques naturally provide this information, if the full complex signal is retained after Fourier transformation. For all the data presented here, we use spectral / Fourier domain OCT (Fercher et al., 1995), which uses a broadband light source and spectrometer. The relative merits of spectral / Fourier domain OCT and swept source OCT for Doppler OCT have been discussed in the literature (Hendargo et al.).

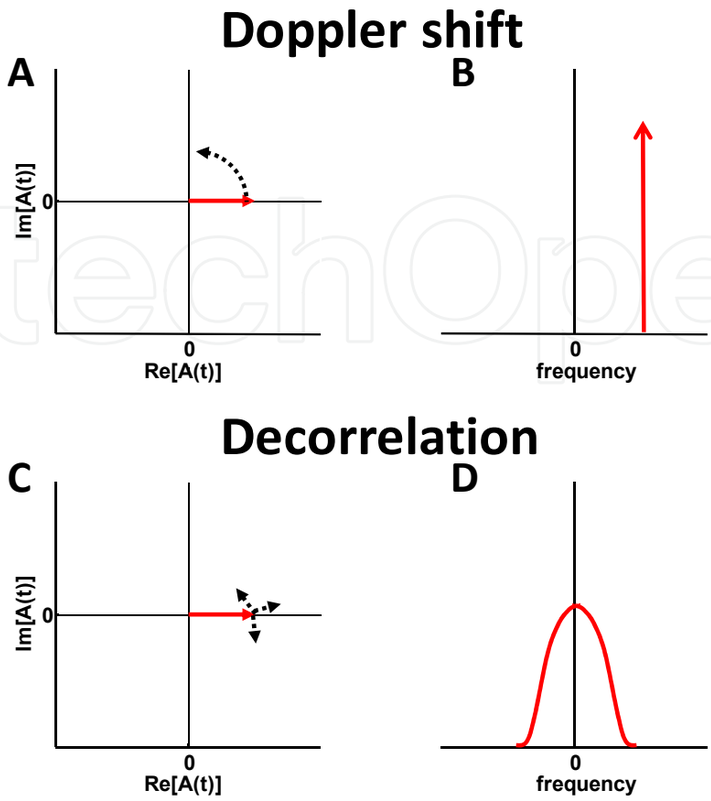

Fig. 1. Qualitative visualization of dynamics in the time and frequency domains. (A-B) Doppler shifting causes a pure rotation of the OCT signal in the complex plane, and leads to a frequency shift of the power spectrum. (C-D) Decorrelation causes random deviations of the OCT signal in the complex plane, and leads to a broadening of the power spectrum. In general, blood flow is accompanied by both Doppler shifts and decorrelation, leading to both shifting and broadening of the power spectrum.

2.2 Theory

The starting point for our discussion is the complex-valued OCT signal, as shown below.

$$A(t) = |A(t)| \exp[j\theta(t)] \quad (1)$$

The complex OCT signal is proportional to the electric field backscattered from scatterers in a voxel. In general, motion of scatterers is accompanied by both 1) Doppler phase shifts (caused by axial translation of a particle) and 2) decorrelation (typically caused by relative translation of a particle and the resolution voxel). Doppler phase shifts can be visualized as rotations of the electric field vector in the complex plane (Fig. 1A-B), while decorrelation can be visualized as random deviations of the electric field vector (Fig. 1C-D). Both Doppler OCT and OCT angiography can be understood from Fig. 1. Doppler OCT measures linear changes in the phase (θ) over time, to infer velocity axial projections. By comparison, OCT angiography generates contrast for moving scatterers based on field deviations in the complex plane.

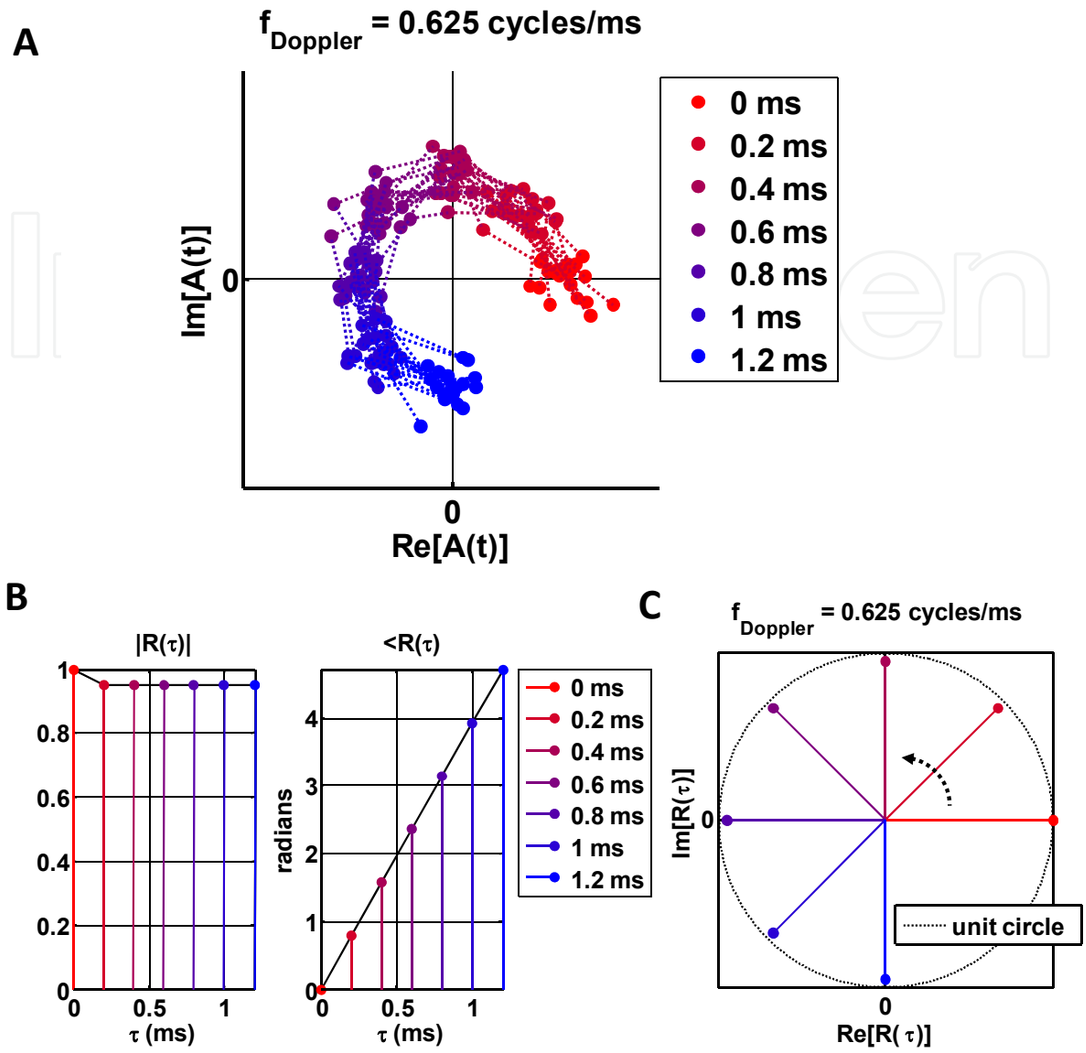

Fig. 2. (A) Visualization of the electric field in the complex plane under additive noise ($SNR=(A_0/\sigma)^2=20$) and Doppler shifting. The model in Eq. (5) was used, with a sampling rate of T=0.2 ms. The phase of the initial time point is set to zero, the amplitude is set to 1, and different time points are color-coded. (B) Magnitude and phase of the normalized autocorrelation function. (C) Rotation of the normalized autocorrelation function in the complex plane. Under additive noise, the distribution spread remains constant over time. For simplicity the effects of static scattering have been neglected ($A_s=0$ in Eq. (2)), and no decorrelation was assumed.

An additional concept required for the discussion of Doppler OCT and OCT angiography is the notion of a three-dimensional resolution voxel. The complex OCT signal (A) can be described as the superposition of a static scattering component (A_s), a dynamic scattering component (A_d), and additive noise (N) (Srinivasan et al., 2010; Yousefi et al., 2011) within a single voxel defined by the axial (z) and transverse (xy) resolutions, as shown below.

$$A(t)=A_s+A_d(t)+N(t) \tag{2}$$

In OCT, the axial image resolution in tissue, Δz, is inversely proportional to the bandwidth of the light source used for imaging as shown below,

$$\Delta z = \frac{2\ln(2)}{\pi n_{group}} \frac{\lambda_0^2}{\Delta\lambda} \tag{3}$$

where $\Delta\lambda$ is the full width half maximum (FWHM) of the light source, n_{group} is the group refractive index in tissue, and λ_0 is the center wavelength of the light source. The transverse resolution is determined by the numerical aperture of focusing as shown below,

$$\Delta x = \Delta y = \frac{\sqrt{2\ln(2)}\lambda_0}{\pi NA} \tag{4}$$

In the above expression, NA is the numerical aperture, as defined for Gaussian beams.

Doppler OCT estimates the angular frequency of the complex OCT signal, whereas angiography generates contrast for moving scatterers based on deviations in the complex OCT signal. In order to understand how these methods operate, it is instructive to develop and visualize simple stochastic models for the complex OCT signal.

The simplest model for the complex OCT signal, shown in Fig. 2, assumes a rotating complex electric field vector with a pure Doppler shift and additive, white noise. Under these conditions, the complex electric field can be represented by the following expression:

$$\begin{aligned} &A(nT) = \exp(j2\pi f_{Doppler} nT) A_0 + N_n \\ &\text{where } N_n \sim \mathbb{N}[0,\sigma^2] \text{ and are i.i.d} \end{aligned} \tag{5}$$

In Eq. (5), $f_{Doppler}$ is the Doppler frequency shift, n is a discrete index, and T is the sampling interval. A_0 is a complex constant. The N_n represent a random process. The N_n are zero-mean, independent, and identically distributed complex Gaussian random variables with a variance of σ^2. The axial projection of velocity v_z is related to the Doppler frequency shift $f_{Doppler}$ as follows:

$$v_z = f_{Doppler} \frac{\lambda_0}{2n_{phase}} \tag{6}$$

where n_{phase} is the phase refractive index in tissue and λ_0 is the center wavelength.

While the additive noise model is intuitive and simple, it is also important to realize that Eq. (5) represents an idealized situation. In reality, so-called "decorrelation noise" (Vakoc et al., 2009) is present. Decorrelation is caused by random deviations in the amplitude and phase from the average path of the electric field in the complex plane. Decorrelation can be caused by translation of the probe beam due to transverse scanning, or translation of scatterers due to blood flow. Decorrelation can also be caused by random amplitude and phase fluctuations from red blood cell orientation or shape changes. Decorrelation may additionally be caused by a random distribution of individual red blood cell velocities, or random deviations in the paths of individual red blood cells from uniform translation, which can be modelled as diffusion (Weitz et al., 1989). Decorrelation has a characteristic

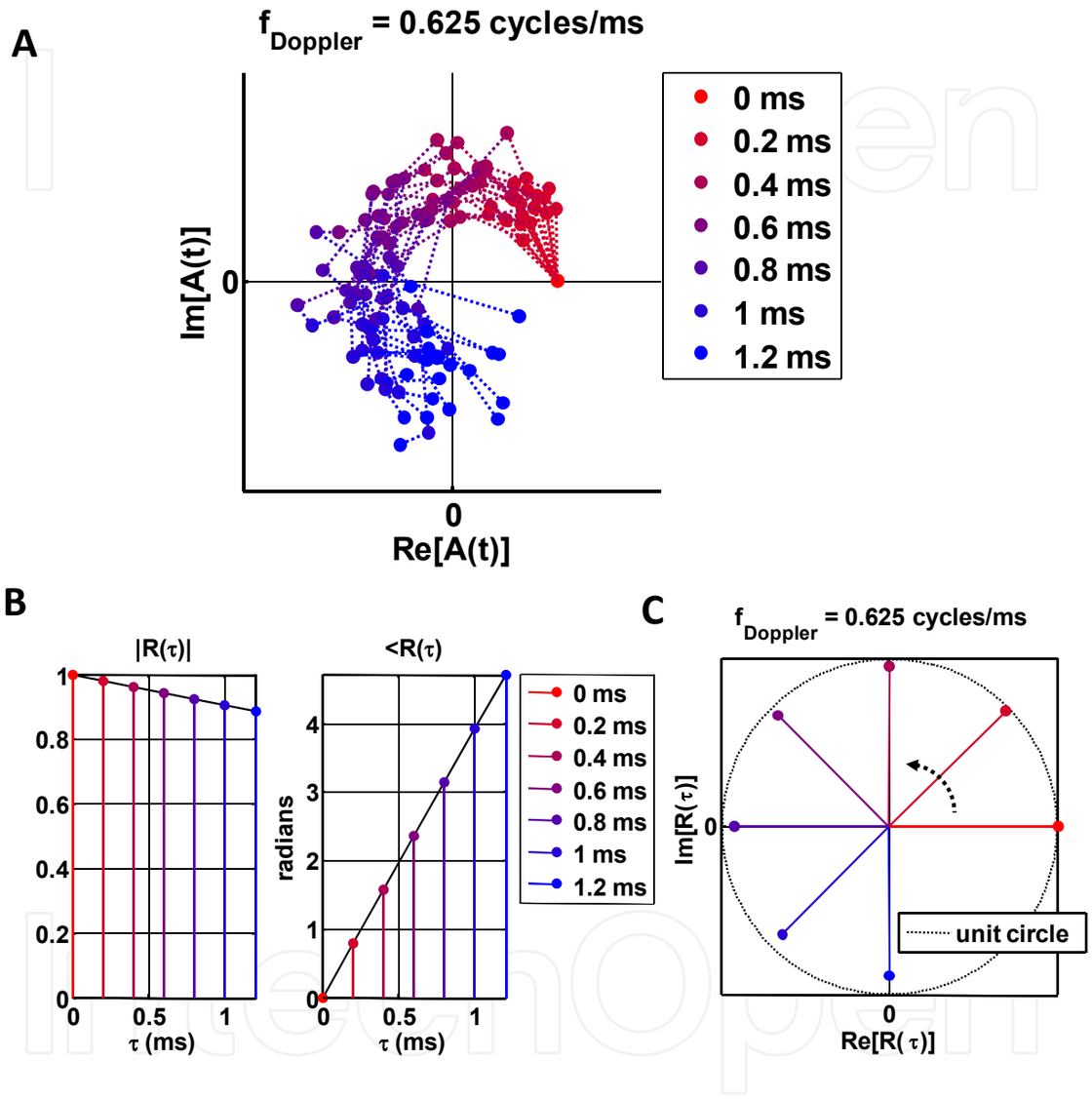

Fig. 3. (A) Visualization of the electric field in the complex plane under both decorrelation and Doppler shifting. The model in Eq. (7) was used, with a sampling rate of T=0.2 ms. The phase of the initial time point is set to zero, the amplitude is set to 1, and different time points are color-coded. (B) Magnitude and phase of the normalized autocorrelation function. (C) Rotation of the normalized autocorrelation function in the complex plane. The distinguishing feature of decorrelation is an increase in the spread of the distribution with time. For simplicity the effects of static scattering and additive noise have been neglected (A_s=0 and N=0 in Eq. (2)).

time scale, known as the decorrelation time, after which the complex amplitude is randomized. In other words, the value of the complex OCT signal at any given time would have no predictive value after the decorrelation time has passed. Under conditions of decorrelation, the complex electric field can be represented by the following model, which represents a Gaussian random process:

$$\begin{aligned} &A[(m+n)T]=\alpha_n \exp(j2\pi f_{Doppler} nT)A[mT]+D_n \\ &\text{where } D_n \sim \mathbb{N}[0,\Sigma]. \end{aligned} \tag{7}$$

The model described in Eq. (7) accounts for both Doppler shifting and decorrelation, and is shown in Fig. 3. The elements of the covariance matrix (Σ_{mn}) can be derived by assuming wide sense stationarity.

$$\begin{aligned} &\Sigma_{mn}=E[D_m D_n^*]= \\ &E[|A|^2]\exp[j2\pi f_{Doppler}(m-n)T][\alpha_{m-n}-\alpha_m \alpha_n] \end{aligned} \tag{8}$$

In the above equations, α_n is a real coefficient with a magnitude between 0 and 1, with $\alpha_0=1$. The autocorrelation function is given by

$$R[nT]=\frac{E\{A^*[mT]A[(m+n)T]\}}{E\{|A|^2\}}=\alpha_n \exp(j2\pi f_{Doppler} nT) \tag{9}$$

Thus the width of α_n determines the decorrelation time. The right side of Eq. (7) can be viewed as a sum of a deterministic component and a random component, where the first term, $\alpha_n \exp(j2\pi f_{Doppler} nT)A[mT]$, represents the deterministic component, and the second term, D_n, represents the random component. As n increases, α_n decreases, and the random component dominates. Therefore, if nT is much larger than the decorrelation time, A[mT] yields no information about A[(m+n)T]. Finally, we note that is possible to model the effects of static scattering by insertion of a constant term in Eq. (5) or (7); however for simplicity we have not included the effects of static scattering here.

2.3 Motion correction

Bulk axial motion is the dominant motion artefact in Doppler OCT. In general, bulk motion causes both a phase shift (White et al., 2003) and an axial image shift (Swanson et al., 1993). For bulk motion on the order of a wavelength, which in turn is much smaller than the axial resolution, the dominant effect of motion is a phase shift. Either galvanometer jitter, thermal drift, or physiologic motion may cause phase shifts. A number of strategies for bulk motion correction have been proposed (Makita et al., 2006; White et al., 2003). Motion correction techniques ideally use a reference (non-vascular) tissue region that can be analyzed to determine the phase shift due to bulk motion. The simplest method to determine the bulk phase shift between two axial scans is to calculate their complex cross-correlation; however, this approach has the disadvantage that it does not account for Doppler shifts from flowing blood. More sophisticated methods use histogram techniques to estimate the bulk phase shift (Yang et al., 2002).

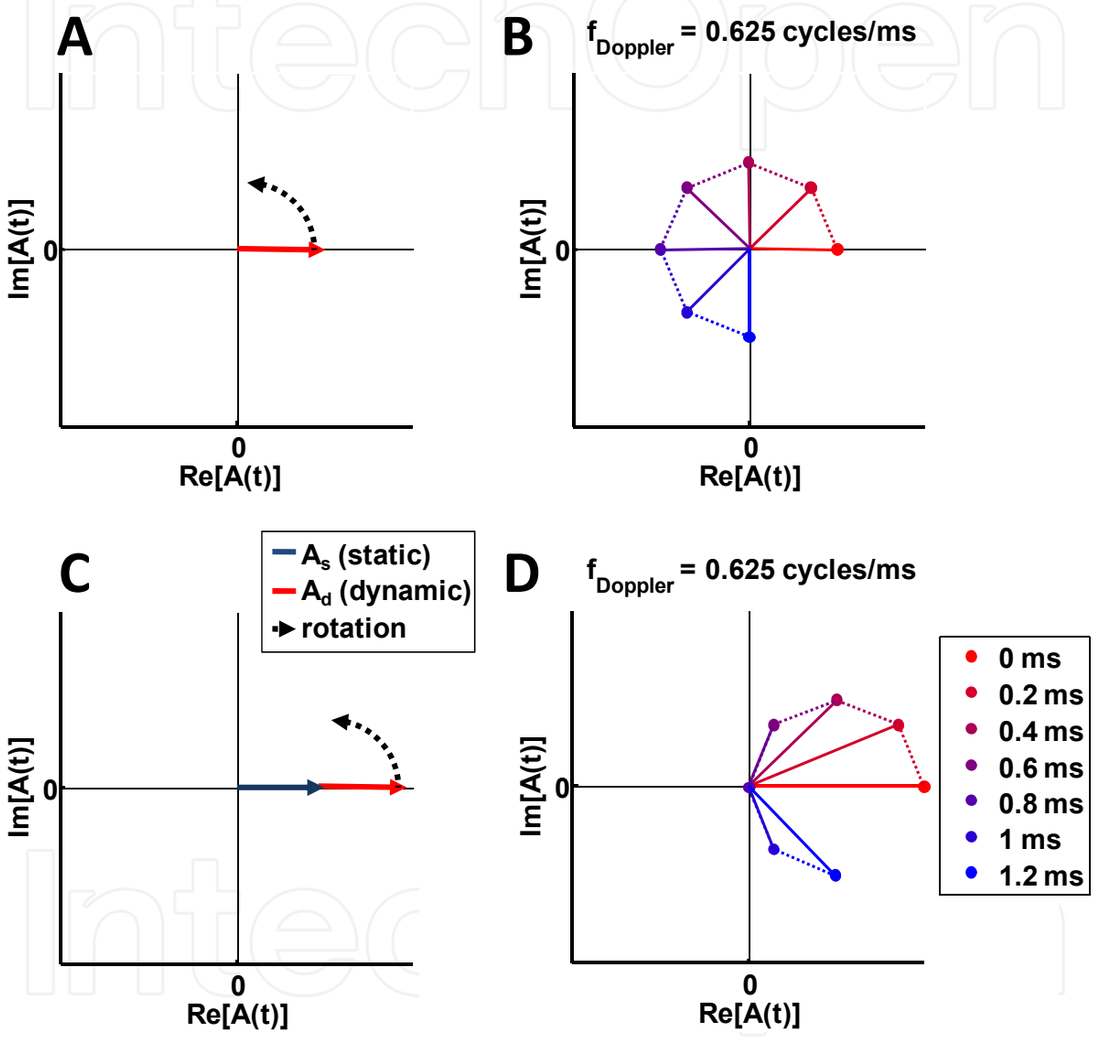

Fig. 4. Static scattering can lead to underestimation of Doppler frequency. (A-B) Visualization of the electric field vector in the complex plane for a pure Doppler shift with no static scattering and no additive noise (A_s=0 and N=0 in Eq. (2)). (C-D) Visualization of the electric field vector in the complex plane for a pure Doppler shift in the presence of static scattering (A_s≠0 and N=0 in Eq. (2)).

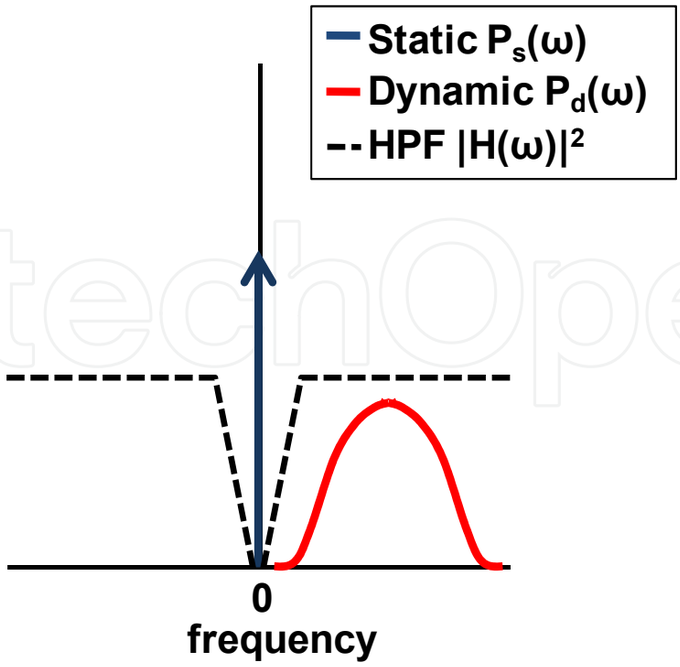

Fig. 5. High-pass filtering is one method to separate static and dynamic scattering components. The static scattering or "D.C." component of the power spectrum is shown in blue, while the dynamic scattering component of the power spectrum is shown in red.

2.4 Isolation of dynamic scattering

Early in the development of high-speed Doppler OCT techniques, the detrimental effect of static scattering on the accuracy of Doppler velocity estimation was recognized. If standard Doppler estimation algorithms are applied in a region with both static and dynamic scattering, the velocity of the dynamic component will be underestimated due to the presence of the static scattering (Ren et al., 2006). This can be seen visually in Fig. 4. Therefore, it is necessary to correctly account for the effects of static scattering in any Doppler estimation procedure. Scattered power from a voxel can be represented as a linear superposition of static and dynamic scattering components (Srinivasan et al., 2010; Tao et al., 2008). In the frequency domain, the power spectrum contains a so-called "D.C" (Tao et al., 2008) or static (Srinivasan et al., 2010) component centered at zero frequency, and a Doppler shifted, broadened component corresponding to dynamic scattering (Srinivasan et al., 2010; Tao et al., 2008; R. K. Wang and An, 2009).

$$P(\omega)=P_s(\omega)+P_d(\omega) \tag{10}$$

Therefore, both the complex OCT signal (Eq. (2)) and the power spectrum (Eq. (10)) can be represented as a superposition of static and dynamic scattering components. If the optical beam is scanned across the tissue, the spectral width of the static scattering component is related to the scanning speed and the transverse resolution (Srinivasan et al., 2010). We will argue that the dynamic scattering component can be estimated by high-pass filtering. Similar filtering techniques can also be found in the ultrasound literature (Bjaerum et al., 2002). Mathematically,

$$A_d(nT) \approx A(nT)*h(nT) \tag{11}$$

In the above equation, h(nT) is the high-pass filter kernel, and * denotes a discrete convolution. Therefore, the power spectrum of the dynamic scattering component is approximately equal to the high-pass filtered power spectrum, as shown below,

$$P_d(\omega) \approx P(\omega)\,|\,H(\omega)\,|^2 \tag{12}$$

Eq. (12) can also be understood intuitively from Fig. 5. After removal of static scattering, estimation algorithms can be applied to determine the Doppler frequency shift, as described below. We also note here that the high-pass filtering operation to remove static scattering, while simple and intuitive, is an *ad hoc* procedure and may result in biased velocity estimates (Srinivasan et al., 2010). Further work in the area of parametric estimation algorithms could directly account for static scattering in the velocity estimation procedure.

2.5 Doppler frequency estimation

A number of Doppler frequency and velocity estimation algorithms have been proposed. However, to date, a comprehensive comparative study on the properties of different estimators (such as bias and mean squared error) has not been performed. Two particular algorithms in widespread use, the Kasai autocorrelation method (Y. Zhao et al., 2000) and the joint spectral and time domain OCT (STdOCT) approach described by Szkulmowski et. al (Szkulmowski et al., 2008), will be discussed.

The Kasai autocorrelation method, as applied to phase-resolved Doppler OCT, first estimates the autocorrelation at a time lag of one sampling period.

$$\hat{R}(T)=\sum_{n=0}^{N-1} A^*[nT]A[(n+1)T] \tag{13}$$

A Kasai window can be defined, over which the estimation is performed. The Doppler frequency is estimated as the phase of the autocorrelation at a time lag of T divided by T.

$$f_{Kasai}=\frac{\angle\hat{R}(T)}{2\pi T} \tag{14}$$

Recently, the technique of joint Spectral and Time domain OCT was proposed (Szkulmowski et al., 2008). In this technique, a series of axial scans are performed at approximately the same transverse position, yielding a time series. The frequency estimate is then chosen as the point in the power spectrum of the time series with the highest amplitude:

$$\hat{\omega}=\arg\max_{\omega\in[-\pi,\pi]}\left\{\hat{P}(\omega)\right\}$$

$$f_{STdOCT}=\frac{\hat{\omega}}{2\pi T} \tag{15}$$

To compare these two methods, it is instructive to view the frequency domain equivalent of the Kasai method. In order to relate the Kasai autocorrelation method to the power spectrum, the autocorrelation estimate can be defined as follows.

$$\hat{R}(nT)=\sum A^{*}[mT]A[(m+n)T] \tag{16}$$

By the Weiner-Khinchin theorem, the autocorrelation and power spectrum are related by a Fourier transformation. The autocorrelation estimate described in Eq. (16) can be thus be approximately related to a power spectrum estimate, shown below.

$$\hat{P}(\omega) \approx \sum_{n=-\infty}^{n=\infty} \hat{R}[nT]e^{-j\omega n} \tag{17}$$

Therefore, the autocorrelation at a time lag of T can be approximately determined with an inverse discrete-time Fourier transformation as shown below.

$$\hat{R}(T) \approx \frac{1}{2\pi}\int_{-\pi}^{\pi} e^{j\omega}\hat{P}(\omega)d\omega \tag{18}$$

Thus, the angle of the autocorrelation at a time lag of T can be loosely viewed as the weighted circular average of frequencies in the power spectrum, where each frequency ω is represented by a complex phasor $e^{j\omega}$ and weighted by the power spectrum estimate at that frequency. Hence the Kasai autocorrelation can be seen as performing a weighted circular average of digital frequencies in the power spectrum, and estimating the frequency using the argument of the result as shown in Eq. (14). By contrast, the joint STdOCT method chooses the frequency with maximum amplitude in the power spectrum for the estimate. The best velocity estimator for a given situation may depend on the noise characteristics, and the relative contributions of additive noise (Fig. 2) versus decorrelation noise (Fig. 3). We do not present a detailed characterization of the different estimators. Desirable characteristics of a good velocity estimator are "unbiasedness" and efficiency. However, to date a systematic study of velocity estimation algorithms in Doppler OCT has not been performed.

3. OCT Angiography

Angiography techniques aim to visualize the lumens of blood vessels. Red blood cells are the predominant cellular scattering component in blood. Therefore, blood vessels are typically visualized as highly scattering regions in standard OCT intensity images. However, smaller blood vessels such as capillaries may be obscured by surrounding highly scattering tissue. Therefore, in order to achieve high contrast angiograms, the contrast of red blood cells must be enhanced relative to that of surrounding tissue. OCT angiography techniques make use of the fact that red blood cell scattering is dynamic, exhibiting phase or amplitude fluctuations over time, while static tissue scattering is relatively constant over time.

Soon after the development of Doppler OCT in the mid to late 1990s, it was recognized that Doppler signals could be used to visualize vasculature (Yonghua Zhao et al., 2000), thus

forming an angiogram of vasculature within tissue. The development of Fourier domain OCT techniques opened the door to high-speed, high-resolution, and volumetric angiography. In 2006, Makita et al. developed techniques to perform Optical Coherence Angiography of the vasculature in the retina and choroid (Makita et al., 2006). Around the same time, moving-scatterer-sensitive OCT was developed to separate static and dynamic scattering in order to achieve more accurate Doppler velocity profiles (Ren et al., 2006). In 2007, Wang et al. further extended these techniques to perform Optical Angiography (OAG) through the intact cranium in anesthetized mice (R. K. Wang and Hurst, 2007; R. K. Wang et al., 2007).

Recent advances in imaging speeds and algorithms have led to high-resolution, large field-of-view imaging of vascular beds down to the capillary level (Srinivasan et al., 2010; Vakoc et al., 2009). A range of techniques are currently used for OCT angiography. Some techniques use the field magnitude (Mariampillai et al., 2010; Mariampillai et al., 2008), others techniques use the phase (Fingler et al., 2007; Vakoc et al., 2009), while other techniques use the complex field (An et al., 2010; Srinivasan et al., 2010; Tao et al., 2008; R. K. Wang et al., 2007), thus incorporating both magnitude and phase information.

Magnitude-based angiography techniques such as speckle variance methods, are based on $|A|$ in Eq. (1). They are insensitive to bulk phase changes, and therefore do not require bulk motion phase correction. Phase-based angiography techniques such as phase variance methods are essentially based on $\exp[j\theta]$ in Eq. (1). They require bulk phase motion correction. Complex-OCT signal based angiography techniques are based on $A= |A|\exp[j\theta]$ in Eq. (1). They also require bulk phase motion correction. Complex angiography can be viewed as high-pass filtering the complex field, which is a superposition of static and dynamic components, as shown in Eq. (2). The goal of angiography is essentially to estimate the power in the dynamic scattering component. This can be accomplished with a high-pass filtering operation, as shown in Fig. 5 and in the expression below,

$$\frac{1}{2\pi}\int_{-\pi}^{\pi} P_d(\omega)d\omega \approx \frac{1}{2\pi}\int_{-\pi}^{\pi} P(\omega)\,|H(\omega)|^2 d\omega \tag{19}$$

High-pass filtering the OCT signal along the slow axis achieves better sensitivity than high-pass filtering along the fast axis, enabling visualization of capillary flow (An et al., 2010; Srinivasan et al., 2010).

Angiography techniques can be understood by visualizing the electric field vector in the complex plane. In general, it is possible to distinguish two types of behavior, which are, in general present to some degree in all voxels. Firstly, axial motion leads to a linear change in the phase of the electric field vector over time (Fig. 2). The rate of phase change, or angular frequency, is used in Doppler OCT to measure particle velocity. A second type of behavior, decorrelation, is characterized by randomization of the complex field over time (Fig. 3). For point particles, decorrelation is caused by motion of the particle through the three-dimensional voxel (defined by Eq. (3) and (4)). Additionally, decorrelation can be caused by a random distribution of axial velocities, leading to a spread (uncertainty) in the angle θ over time. For red blood cells (biconcave disks with diameter of 6-8 microns and an aspect ratio of approximately 4), one would expect significant anisotropy in the scattering phase function. Therefore, decorrelation may be caused by red blood cell orientation changes as

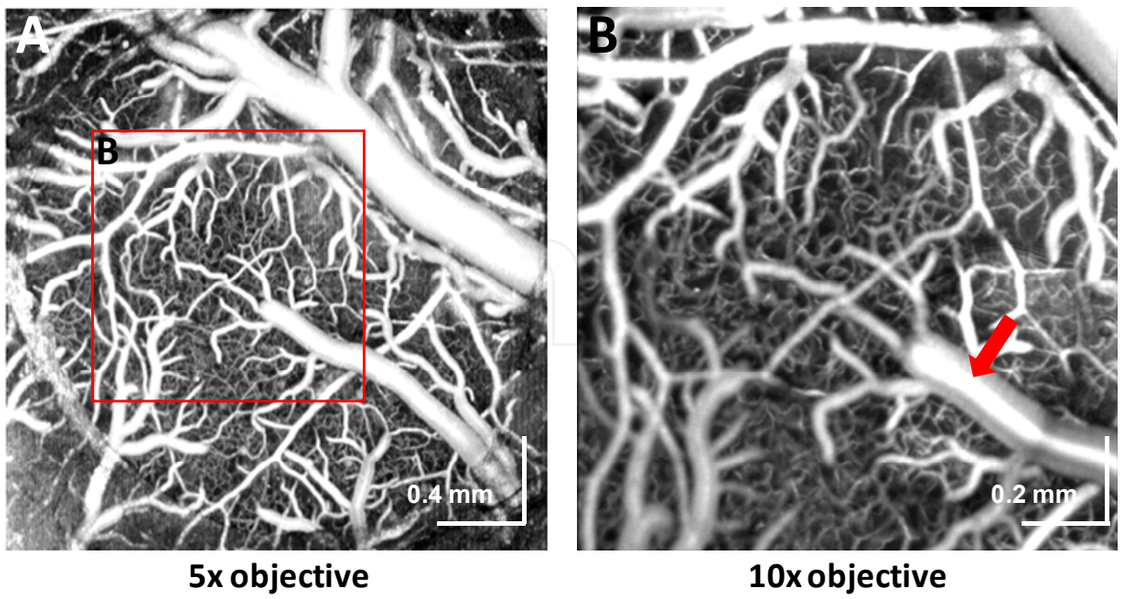

Fig. 6. OCT angiography in the rat parietal cortex through a closed cranial window. At a transverse resolution of 7 microns, the entire 3 mm window is imaged (A). At a transverse resolution of 3.5 microns, detailed microvasculature is imaged over a smaller field of view (B). The red arrow in B shows a bright "stripe" pattern along the center axis of a vein, due to the shear-induced orientation of the flat face of the red blood cells perpendicular to the probe beam.

well. In general, angiography can visualize regions with either Doppler shifting or decorrelation, since both behaviours result in power being shifted to higher frequencies (Fig. 1).

4. Absolute blood flow measurements

Blood flow is a fundamental physiological parameter. Classical methods to quantify cerebral blood flow, pioneered by Kety and colleagues (Kety, 1951), introduce a foreign, chemically inert tracer that diffuses freely across the blood brain barrier. Similar concepts are used in MRI arterial spin labeling and PET radiotracer methods to quantify perfusion.

Traditional optical imaging methods such as laser speckle and laser Doppler imaging do not provide absolute blood flow measurements. Doppler OCT has the capability to perform absolute blood flow measurements based on Doppler shifted light backscattered from moving red blood cells. Phase-resolved Doppler OCT (Yonghua Zhao et al., 2000) has become the method of choice due to its high velocity sensitivity and compatibility with Fourier domain OCT techniques. In particular, one can imagine a hypothetical three-dimensional incompressible vector field $\mathbf{v}(x,y,z)$, which gives the spatially-resolved velocity profile within vessels, and is zero outside vessels. Flow in a vessel can be interpreted as the flux of $\mathbf{v}(x,y,z)$ through any surface bisecting the vessel. Ideally, Doppler OCT measures the axial or z-projection of this three-dimensional vector field, i.e. $v_z(x,y,z)$. Therefore, flow in any vessel can be obtained from the Doppler OCT data by calculating the velocity flux through the *en*

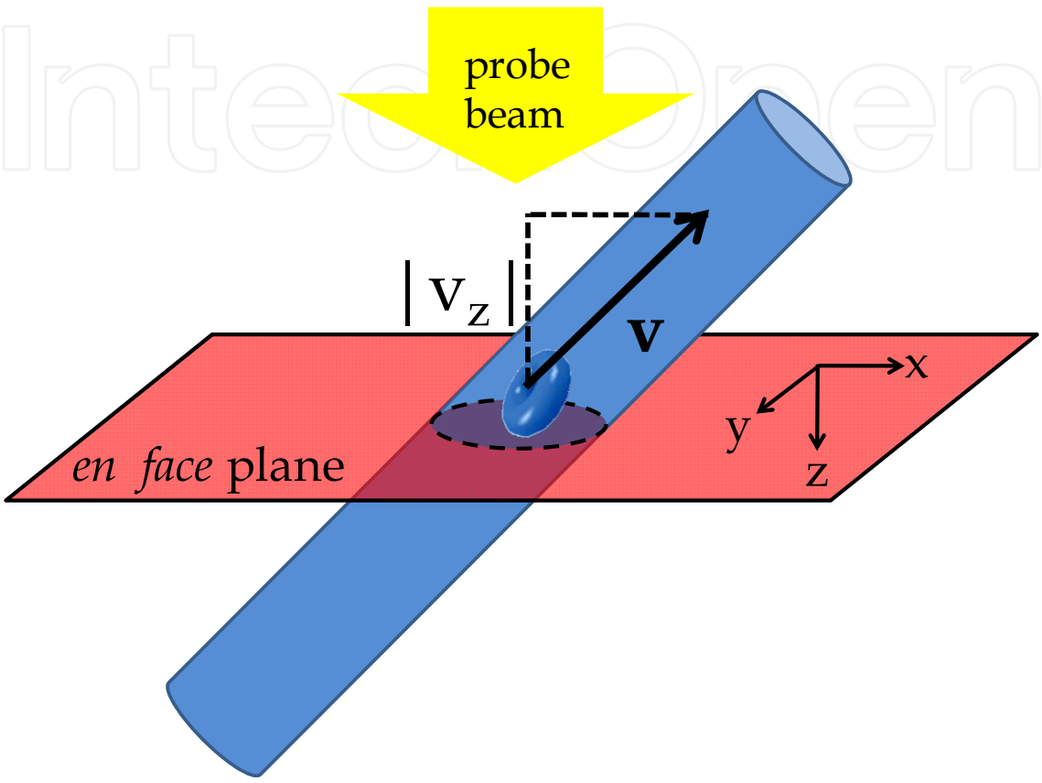

Fig. 7. Geometry for flow calculation using Doppler OCT. An ascending vessel with flow towards the incident probe beam is bisected by the *en face* plane. A red blood cell is shown, with a velocity vector given by **v**, while the magnitude of the velocity axial (z) projection is given by $|v_z|$.

face (also known as transverse or xy) plane using the following expression, (Srinivasan et al., 2010)

$$F = \iint_{ROI} v_z(x,y,z_0)\,dxdy \tag{20}$$

The ROI for integration is chosen to encircle the cross-section of the vessel in a particular *en face* plane, as shown in Fig. 7. Thus, by judicious choice of the surface for integration perpendicular to the measured velocity component, explicit calculation of vessel angles (Y. Wang et al., 2007) is not required to determine flow. To understand why this simple procedure works, note that Eq. (20) can be rewritten as the product of the cross-sectional area in the *en face* plane and the mean velocity axial projection.

$$F = A_{xy}\,\overline{v_z} \tag{21}$$

The cross-sectional area in the *en face* plane is given by

$$A_{xy} = \iint_{ROI} dxdy\,, \tag{22}$$

and the mean velocity axial projection is given by

$$\overline{v_z} = \iint_{ROI} v_z(x,y,z_0)dxdy \Big/ \iint_{ROI} dxdy\,. \tag{23}$$

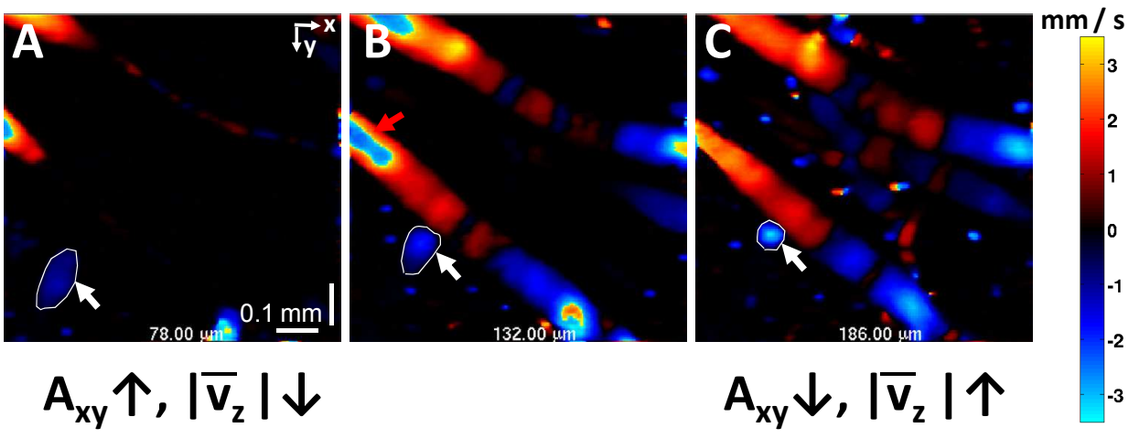

Fig. 8. Flow is conserved in a non-branching vessel. A single ascending vein at a depth (z_0) of 78 µm (A), 132 µm (B), and 186 µm (C) is shown. With increasing depth, as the vessel orientation becomes more axial, the vessel cross-sectional area (demarcated by white ROIs) in the *en face* plane decreases. At the same time, with increasing depth, the mean velocity axial projection increases in magnitude. As a result, flow, calculated as the product of these two quantities (Eq. (21)), is conserved. A region with aliasing of velocities is marked by a red arrow in B.

Keeping these equations in mind, it is instructive to view Doppler OCT images of a cortical vessel in *en face* planes at different depths, as in Fig. 8A, B, and C (z_0 = 78, 132, and 186 µm respectively). An ascending vein is demarcated by whites ROIs at each depth. Since flow in a vein drains the cortex, and by convention the +z direction points into the cortex, velocity axial projections are negative in veins. Therefore, according to Eq. (20), flow in veins is

negative and flow in arteries is positive. With increasing cortical depth, the ascending vein changes from a more transverse (A) to a more axial (C) orientation. As the vein becomes more axially oriented (more parallel to the probe beam), the cross-sectional area in the *en face* plane is reduced (Eq. (22)), while the magnitude of the mean velocity axial projection is increased (Eq. (23)). Due to the fact that transverse cross-sectional area and velocity axial projection change in opposing directions, flow (as computed in Eq. (21)) is conserved. Similar methods of flow calculation, that, for instance, use an angiogram to determine the cross-sectional area in the *en face* plane more accurately, are also possible. The concept of *en face* integration to determine flow could be applied to ultrasound as well.

Using this method of flow calculation, conservation at branch points and along non-branching segments has been demonstrated (Srinivasan et al., 2011). Furthermore, Doppler OCT flow values correlated with hydrogen clearance flow values when both were measured simultaneously across multiple subjects. The technique of *en face* integration has recently been adapted to measure total retinal blood flow (Baumann et al., 2011) and glomerular blood flow (Wierwille et al., 2011).

However, there are limitations to Doppler OCT blood flow measurements. First, flow measurements are accurate only in vessels with a well-defined flow profile. Flow values are most accurate in large arteries and veins, but flow calculations necessarily fail in capillaries where the red blood cells flow in a single file. Second, the RBC velocity axial projection profile (measured by Doppler OCT) may not reflect the true flow profile, as there is an "RBC-free" zone at the periphery of the vessel lumen. Third, the presence of static scattering and dynamic scattering within voxels at the edge of vessels must be addressed by filtering or fitting techniques. Fourth, vessels must be measured at locations where they generate a Doppler shift above the detection threshold. Therefore, Doppler methods would fail where a vessel is perpendicular to the probe beam, or where velocity axial projections are not sufficiently large. Fifth, Doppler OCT relies on scattering from red blood cells, and flow measurements would therefore be inaccurate under conditions of extremely low hematocrit. Nevertheless, Doppler OCT flowmetry is non-invasive and correlates with gold standard absolute flow values across subjects (Srinivasan et al., 2011). These features make Doppler OCT an attractive technique for non-invasive longitudinal, high resolution blood flow imaging.

5. Conclusion

In conclusion, Doppler OCT and OCT angiography are complementary tools to quantitatively study vascular physiology. OCT occupies an important niche between diffuse optical imaging methods and invasive microscopic techniques. A novel technique of absolute blood flow measurement with Doppler OCT, which does not require explicit calculation of vessel angles, was recently validated in the brain (Srinivasan et al., 2011) and shown to provide flow measurements within a reasonable physiological range. This technique was recently applied in the retina (Baumann et al.) and in the kidney glomeruli (Wierwille et al., 2011). These non-invasive optical imaging technologies promise to advance longitudinal imaging of blood flow in living organ systems for basic and translational research.

6. Acknowledgment

We acknowledge support from the NIH (K99NS067050), the AHA (11IRG5440002), and the Glaucoma Research Foundation. We also acknowledge conversations with Cenk Ayata, Jonghwan Lee, Eng Lo, David Boas, Weicheng Wu, Lana Ruvinskaya, Alex Cable, James Jiang, Sava Sakadzic, Mohammed Abbas Yaseen, James Fujimoto, Iwona Gorczynska, Emiri Mandeville, and Harsha Radhakrishnan.

7. References

An, L., Qin, J., and Wang, R. K., "Ultrahigh sensitive optical microangiography for in vivo imaging of microcirculations within human skin tissue beds," Opt Express 18, 8220-8228 (2010).

Baumann, B., Potsaid, B., Kraus, M. F., Liu, J. J., Huang, D., Hornegger, J., Cable, A. E., Duker, J. S., and Fujimoto, J. G., "Total retinal blood flow measurement with ultrahigh speed swept source/Fourier domain OCT," Biomed Opt Express 2, 1539-1552 (2011).

Bjaerum, S., Torp, H., and Kirstoffersen, K., "Clutter filter design for ultrasound color flow imaging," IEEE Trans. Ultrason. Ferroelectr. Freq. Control 49, 204-216 (2002).

Chen, Z., Milner, T. E., Dave, D., and Nelson, J. S., "Optical Doppler tomographic imaging of fluid flow velocity in highly scattering media," Optics Letters 22, 64-66 (1997).

Choma, M. A., Sarunic, M. V., Yang, C. H., and Izatt, J. A., "Sensitivity advantage of swept source and Fourier domain optical coherence tomography," Optics Express 11, 2183-2189 (2003).

de Boer, J. F., Cense, B., Park, B. H., Pierce, M. C., Tearney, G. J., and Bouma, B. E., "Improved signal-to-noise ratio in spectral-domain compared with time-domain optical coherence tomography," Opt Lett 28, 2067-2069 (2003).

Denk, W., Strickler, J. H., and Webb, W. W., "2-Photon Laser Scanning Fluorescence Microscopy," Science 248, 73-76 (1990).

Dirnagl, U., Kaplan, B., Jacewicz, M., and Pulsinelli, W., "Continuous measurement of cerebral cortical blood flow by laser-Doppler flowmetry in a rat stroke model," J Cereb Blood Flow Metab 9, 589-596 (1989).

Dunn, A. K., Bolay, H., Moskowitz, M. A., and Boas, D. A., "Dynamic imaging of cerebral blood flow using laser speckle," J Cereb Blood Flow Metab 21, 195-201 (2001).

Fercher, A. F., Hitzenberger, C. K., Kamp, G., and El-Zaiat, S. Y., "Measurement of intraocular distances by backscattering spectral interferometry," Opt. Commun. 117, 43-48 (1995).

Fingler, J., Schwartz, D., Yang, C., and Fraser, S. E., "Mobility and transverse flow visualization using phase variance contrast with spectral domain optical coherence tomography," Opt Express 15, 12636-12653 (2007).

Golubovic, B., Bouma, B. E., Tearney, G. J., and Fujimoto, J. G., "Optical frequency-domain reflectometry using rapid wavelength tuning of a Cr4+:forsterite laser," Opt Lett 22, 1704-1706 (1997).

Grinvald, A., Lieke, E., Frostig, R. D., Gilbert, C. D., and Wiesel, T. N., "Functional architecture of cortex revealed by optical imaging of intrinsic signals," Nature 324, 361-364 (1986).

Hendargo, H. C., McNabb, R. P., Dhalla, A. H., Shepherd, N., and Izatt, J. A., "Doppler velocity detection limitations in spectrometer-based versus swept-source optical coherence tomography," Biomed Opt Express 2, 2175-2188 (2011).

Hillman, E. M., Boas, D. A., Dale, A. M., and Dunn, A. K., "Laminar optical tomography: demonstration of millimeter-scale depth-resolved imaging in turbid media," Opt Lett 29, 1650-1652 (2004).

Huang, D., Swanson, E. A., Lin, C. P., Schuman, J. S., Stinson, W. G., Chang, W., Hee, M. R., Flotte, T., Gregory, K., Puliafito, C. A., and Fujimoto, J. G., "Optical Coherence Tomography," Science 254, 1178-1181 (1991).

Izatt, J. A., Kulkami, M. D., Yazdanfar, S., Barton, J. K., and Welch, A. J., "In vivo bidirectional color Doppler flow imaging of picoliter blood volumes using optical coherence tomography," Optics Letters 22, 1439-1441 (1997).

Kety, S. S., "The theory and applications of the exchange of inert gas at the lungs and tissues," Pharmacol Rev 3, 1-41 (1951).

Leitgeb, R., Hitzenberger, C. K., and Fercher, A. F., "Performance of Fourier domain vs. time domain optical coherence tomography," Optics Express 11, 889-894 (2003).

Makita, S., Hong, Y., Yamanari, M., Yatagai, T., and Yasuno, Y., "Optical coherence angiography," Optics Express 14, 7821-7840 (2006).

Mariampillai, A., Leung, M. K., Jarvi, M., Standish, B. A., Lee, K., Wilson, B. C., Vitkin, A., and Yang, V. X., "Optimized speckle variance OCT imaging of microvasculature," Opt Lett 35, 1257-1259 (2010).

Mariampillai, A., Standish, B. A., Moriyama, E. H., Khurana, M., Munce, N. R., Leung, M. K., Jiang, J., Cable, A., Wilson, B. C., Vitkin, I. A., and Yang, V. X., "Speckle variance detection of microvasculature using swept-source optical coherence tomography," Opt Lett 33, 1530-1532 (2008).

Ren, H., Sun, T., MacDonald, D. J., Cobb, M. J., and Li, X., "Real-time in vivo blood-flow imaging by moving-scatterer-sensitive spectral-domain optical Doppler tomography," Opt Lett 31, 927-929 (2006).

Srinivasan, V. J., Atochin, D. N., Radhakrishnan, H., Jiang, J. Y., Ruvinskaya, S., Wu, W., Barry, S., Cable, A. E., Ayata, C., Huang, P. L., and Boas, D. A., "Optical coherence tomography for the quantitative study of cerebrovascular physiology," J Cereb Blood Flow Metab 31, 1339-1345 (2011).

Srinivasan, V. J., Jiang, J. Y., Yaseen, M. A., Radhakrishnan, H., Wu, W., Barry, S., Cable, A. E., and Boas, D. A., "Rapid volumetric angiography of cortical microvasculature with optical coherence tomography," Opt Lett 35, 43-45 (2010).

Srinivasan, V. J., Sakadzic, S., Gorczynska, I., Ruvinskaya, S., Wu, W., Fujimoto, J. G., and Boas, D. A., "Quantitative cerebral blood flow with optical coherence tomography," Opt Express 18, 2477-2494 (2010).

Swanson, E. A., Izatt, J. A., Hee, M. R., Huang, D., Lin, C. P., Schuman, J. S., Puliafito, C. A., and Fujimoto, J. G., "In vivo retinal imaging by optical coherence tomography," Opt Lett 18, 1864-1866 (1993).

Szkulmowski, M., Szkulmowska, A., Bajraszewski, T., Kowalczyk, A., and Wojtkowski, M., "Flow velocity estimation using joint Spectral and Time domain Optical Coherence Tomography," Opt Express 16, 6008-6025 (2008).

Tao, Y. K., Davis, A. M., and Izatt, J. A., "Single-pass volumetric bidirectional blood flow imaging spectral domain optical coherence tomography using a modified Hilbert transform," Opt Express 16, 12350-12361 (2008).

Vakoc, B. J., Lanning, R. M., Tyrrell, J. A., Padera, T. P., Bartlett, L. A., Stylianopoulos, T., Munn, L. L., Tearney, G. J., Fukumura, D., Jain, R. K., and Bouma, B. E., "Three-dimensional microscopy of the tumor microenvironment in vivo using optical frequency domain imaging," Nat Med 15, 1219-1223 (2009).

Vakoc, B. J., Tearney, G. J., and Bouma, B. E., "Statistical properties of phase-decorrelation in phase-resolved Doppler optical coherence tomography," IEEE Trans Med Imaging 28, 814-821 (2009).

Villringer, A. and Chance, B., "Non-invasive optical spectroscopy and imaging of human brain function," Trends in Neurosciences 20, 435-442 (1997).

Wang, R. K. and An, L., "Doppler optical micro-angiography for volumetric imaging of vascular perfusion in vivo," Opt Express 17, 8926-8940 (2009).

Wang, R. K. and Hurst, S., "Mapping of cerebro-vascular blood perfusion in mice with skin and skull intact by Optical Micro-AngioGraphy at 1.3 mu m wavelength," Optics Express 15, 11402-11412 (2007).

Wang, R. K., Jacques, S. L., Ma, Z., Hurst, S., Hanson, S. R., and Gruber, A., "Three dimensional optical angiography," Optics Express 15, 4083-4097 (2007).

Wang, Y., Bower, B. A., Izatt, J. A., Tan, O., and Huang, D., "In vivo total retinal blood flow measurement by Fourier domain Doppler optical coherence tomography," Journal of biomedical optics 12, 041215 (2007).

Weitz, D. A., Pine, D. J., Pusey, P. N., and Tough, R. J., "Nondiffusive Brownian motion studied by diffusing-wave spectroscopy," Phys Rev Lett 63, 1747-1750 (1989).

White, B. R., Pierce, M. C., Nassif, N., Cense, B., Park, B. H., Tearney, G. J., Bouma, B. E., Chen, T. C., and de Boer, J. F., "In vivo dynamic human retinal blood flow imaging using ultra-high-speed spectral domain optical Doppler tomography," Optics Express 11, 3490-3497 (2003).

Wierwille, J., Andrews, P. M., Onozato, M. L., Jiang, J., Cable, A., and Chen, Y., "In vivo, label-free, three-dimensional quantitative imaging of kidney microcirculation using Doppler optical coherence tomography," Laboratory investigation; a journal of technical methods and pathology (2011).

Wilt, B. A., Burns, L. D., Ho, E. T. W., Ghosh, K. K., Mukamel, E. A., and Schnitzer, M. J., "Advances in Light Microscopy for Neuroscience," Annual Review of Neuroscience 32, 435-506 (2009).

Yang, V. X. D., Gordon, M. L., Mok, A., Zhao, Y. H., Chen, Z. P., Cobbold, R. S. C., Wilson, B. C., and Vitkin, I. A., "Improved phase-resolved optical Doppler tomography using the Kasai velocity estimator and histogram segmentation," Opt. Commun. 208, 209-214 (2002).

Yousefi, S., Zhi, Z., and Wang, R., "Eigendecomposition-Based Clutter Filtering Technique for Optical Micro-Angiography," IEEE Trans Biomed Eng (2011).

Yun, S., Tearney, G., de Boer, J., Iftimia, N., and Bouma, B., "High-speed optical frequency-domain imaging," Opt Express 11, 2953-2963 (2003).

Zhao, Y., Chen, Z., Saxer, C., Shen, Q., Xiang, S., de Boer, J. F., and Nelson, J. S., "Doppler standard deviation imaging for clinical monitoring of in vivo human skin blood flow," Opt Lett 25, 1358-1360 (2000).

Zhao, Y., Chen, Z., Saxer, C., Xiang, S., de Boer, J. F., and Nelson, J. S., "Phase-resolved optical coherence tomography and optical Doppler tomography for imaging blood flow in human skin with fast scanning speed and high velocity sensitivity," Optics Letters 25, 114-116 (2000).

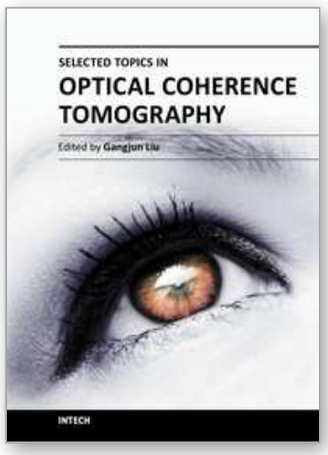

Selected Topics in Optical Coherence Tomography

Edited by Dr. Gangjun Liu

ISBN 978-953-51-0034-8
Hard cover, 280 pages
Publisher InTech
Published online 08, February, 2012
Published in print edition February, 2012

This book includes different exciting topics in the OCT fields, written by experts from all over the world. Technological developments, as well as clinical and industrial applications are covered. Some interesting topics like the ultrahigh resolution OCT, the functional extension of OCT and the full field OCT are reviewed, and the applications of OCT in ophthalmology, cardiology and dentistry are also addressed. I believe that a broad range of readers, such as students, researchers and physicians will benefit from this book.

How to reference

In order to correctly reference this scholarly work, feel free to copy and paste the following:

Vivek J. Srinivasan, Aaron C. Chan and Edmund Y. Lam (2012). Doppler OCT and OCT Angiography for In Vivo Imaging of Vascular Physiology, Selected Topics in Optical Coherence Tomography, Dr. Gangjun Liu (Ed.), ISBN: 978-953-51-0034-8, InTech, Available from: http://www.intechopen.com/books/selected-topics-in-optical-coherence-tomography/doppler-oct-and-oct-angiography-for-in-vivo-imaging-of-vascular-physiology

INTECH
open science | open minds

InTech Europe
University Campus STeP Ri
Slavka Krautzeka 83/A
51000 Rijeka, Croatia
Phone: +385 (51) 770 447
Fax: +385 (51) 686 166
www.intechopen.com

InTech China
Unit 405, Office Block, Hotel Equatorial Shanghai
No.65, Yan An Road (West), Shanghai, 200040, China
中国上海市延安西路65号上海国际贵都大饭店办公楼405单元
Phone: +86-21-62489820
Fax: +86-21-62489821

IntechOpen